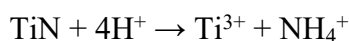


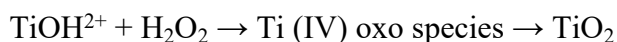
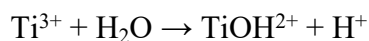
Supplementary Information

Experimental Section

Materials: All reagents were utilized without any additional purification. Titanium nitride (TiN), sodium citrate dihydrate ($C_6H_5Na_3O_7 \cdot 2H_2O$), potassium hydroxide (KOH), sodium hypochlorite (NaClO), ammonium- ^{15}N chloride ($^{15}NH_4Cl$, 98.5%), potassium nitrate- ^{15}N (98.5% $K^{15}NO_3$), salicylic acid ($C_7H_6O_3$), nitroferricyanide (III) dihydrate ($Na_2Fe(CN)_5NO \cdot 2H_2O$), maleic acid ($C_4H_4O_4$), and deuterium oxide (D_2O) were obtained from Shanghai Macklin Biochemical Co., Ltd. Hydrochloric acid (HCl), hydrogen peroxide (H_2O_2 , 30 wt%), iron (II) sulfate heptahydrate ($FeSO_4 \cdot 7H_2O$), ammonium chloride (NH_4Cl), sodium chloride (NaCl), and potassium nitrate (KNO_3) were purchased from Sinopharm Chemical Reagent Co., Ltd. Sodium hydroxide (NaOH) was purchased from Aladdin. Ethanol was purchased from Tianjin Fuyu Fine Chemical Co., Ltd. Deionized water with the resistivity of 18.2 $m\Omega$ was used in all experiments.

Preparation of TiO_2 : TiO_2 was synthesized using TiN as the precursor via a modified hydrothermal method from previously reported literature.¹ In details, 80 mg of TiN were dissolved in a mixed solution of HCl (13 mL, 5 M) and H_2O_2 (5 mL, 30 wt%) using ultrasonic treatment. The mixture was transferred into a 50 mL Teflon-lined stainless-steel autoclave. A piece of carbon paper (CP) (2.5 cm \times 3.0 cm) was vertically placed within the autoclave. After sealing, the autoclave was heated to 200 °C and maintained at this temperature for 20 h. Upon completion of the reaction, the autoclave was naturally cooled to room temperature. TiO_2/CP was subsequently washed alternately with deionized water and ethanol, and finally dried under vacuum at 60 °C. The reaction principle can be explained as follows: a high concentration of H^+ promotes the dissolution of TiN to release Ti^{3+} in an acidic hydrothermal environment. Due to its instability in aqueous solutions, Ti^{3+} undergoes hydrolysis to generate $TiOH^{2+}$, which subsequently reacts with H_2O_2 to convert into Ti^{4+} species, forming TiO_2 .^{2,3} The reaction equations that occur are as follows:





Preparation of TiO₂/Fe: The TiO₂/Fe heterostructure nanorod arrays were synthesized on CP by electrodeposition method using a two-electrode configuration. A piece of TiO₂/CP (1.0 cm × 1.0 cm) was used as the working electrode, and a graphite rod was employed as the counter electrode. The electrodeposition solution comprised FeSO₄·7H₂O (4 mM), NH₄Cl (8 mM), NaCl (8 mM), and C₆H₅Na₃O₇·2H₂O (3.2 mM). The process was conducted under galvanostatic conditions at 50 mA cm⁻² for 60 s.

Preparation of Fe: Fe nanoparticles were synthesized on CP using the similar method as TiO₂/Fe except that TiO₂/CP electrode was replaced with pure CP.

Characterization: X-ray diffraction (XRD) patterns were obtained using Rigaku Smartlab powder diffractometer with a Cu K_α source (λ = 1.5418 Å). Scanning electron microscopy (SEM) images were taken with GeminiSEM 500. Transmission electron microscopy (TEM) images were obtained using HITACHI H-8100, operated at a voltage of 100 kV. High resolution TEM (HRTEM), high-angle annular dark field scanning TEM (HAADF-STEM) and elemental mappings were obtained using JEOL 2100F with an operating voltage of 200 kV. X-ray photoelectron spectroscopy (XPS) spectrum was acquired utilizing an ESCALAB MK II spectrometer with exciting source of Mg. The binding energies were calibrated against the C 1s peak at 284.8 eV. Energy-dispersive X-ray spectroscopy (EDS) were recorded on FEI Talos F200x. Ultraviolet-visible (UV-Vis) absorbance spectra were measured on SHIMADZU UV-1900 spectrophotometer. ¹H nuclear magnetic resonance (NMR) spectra were captured on a Bruker Avance spectrometer operating at 500 MHz. Electron spin resonance (ESR) spectra were obtained using a Bruker-A300 spectrometer. *In-situ* attenuated total reflection Fourier transformed infrared (ATR-FTIR) measurements were conducted by a Thermo Scientific Nicolet 6700 spectrometer.

Electrochemical measurements: All electrochemical measurements were conducted utilizing an electrochemical workstation (CHI760E, Chenhua). A three-electrode setup was employed (TiO₂/Fe on CP for working electrode, Hg/HgO for reference electrode, and Pt foil for counter electrode). The electrolyte contained 1.0 M KOH and 0.1 M

NO_3^- . All potentials reported have been converted to the reversible hydrogen electrode (RHE) according to the equation: E (V vs. RHE) = E (V vs. Hg/HgO) + 0.098 + 0.059 \times pH.

Determination of NH_4^+ concentration: The concentration of NH_4^+ was determined by an indophenol blue method. Initially, 100 μL of electrolyte were extracted from the electrolytic cell and diluted to 10 mL. Subsequently, 2 mL of the diluted electrolyte were taken and mixed with 2 mL of chromogenic agent (1 M NaOH solution containing 5 wt% $\text{C}_7\text{H}_6\text{O}_3$ and 5 wt% $\text{C}_6\text{H}_5\text{Na}_3\text{O}_7 \cdot 2\text{H}_2\text{O}$), 1 mL of oxidizing agent (0.05 M NaClO), and 0.2 mL of 1 wt% $\text{Na}_2[\text{Fe}(\text{NO})(\text{CN})_5] \cdot 2\text{H}_2\text{O}$. After incubating for 2 h at room temperature, the absorbance at wavelength of 655 nm (A) was determined by UV-Vis spectroscopy. The UV-Vis spectra of a series of standard NH_4^+ solutions with known concentrations (c) were measured for calibration ($A = 7.195c + 0.033$, $R^2 = 0.999$).

Determination of NO_3^- concentration: The concentration of NO_3^- was determined by a colorimetric method. Initially, 50 μL of electrolyte were extracted from the electrolytic cell and were diluted to 10 mL. Subsequently, 3 mL of the diluted electrolyte were taken out and mixed with 4 mL of 0.5 M H_2SO_4 . After aging at room temperature for 15 min, UV-Vis spectra were acquired, and the absorbances at wavelengths of 220 nm ($A_{220\text{nm}}$) and 275 nm ($A_{275\text{nm}}$) were recorded. The absorbance of NO_3^- (A) was calculated using the following equation: $A = A_{220\text{nm}} - 2 \times A_{275\text{nm}}$. The calibration curve depicting the relationship between NO_3^- concentration (c) and absorbance was plotted by testing a series of standard KNO_3 solutions ($A = 1.469c + 0.004$, $R^2 = 0.999$).

Calculation of NH_3 yield rate (Y_{NH_3}), Faradaic efficiency (FE_{NH_3}), NH_3 partial current density (j_{NH_3}), and half-cell energy efficiency (EE_{NH_3}):

$$Y_{\text{NH}_3} = \frac{c_{\text{NH}_3} \times V}{t \times S} \quad \#(1)$$

$$FE_{\text{NH}_3} = \frac{8 \times F \times c_{\text{NH}_3} \times V}{Q} \times 100\% \quad \#(2)$$

$$j_{\text{NH}_3} = \frac{Q \times FE_{\text{NH}_3}}{t \times S} \quad \#(3)$$

$$EE_{\text{NH}_3} = \frac{(1.23 - E_{\text{NH}_3}^0) \times FE_{\text{NH}_3}}{1.23 - E} \times 100\% \quad \#(4)$$

where c_{NH_3} (mmol L⁻¹) is the NH₃ concentration, V (L) is the volume of cathode electrolyte, t (h) is the reduction time, S (cm²) is the geometric area of working electrode, F (96485 C mol⁻¹) is the Faradaic constant, Q (C) is the amount of charge consumed during chronoamperometry test, $E_{\text{NH}_3}^0$ represents the equilibrium potential of nitrate reduction to ammonia (0.69 V), and E is the applied potential.

Calculation of electrochemical active surface area (ECSA):

$$\text{ECSA} = \frac{C_{\text{dl}}}{C_s} \quad \#(5)$$

where C_s is the specific capacitance for a flat metallic surface (40 μF cm⁻²),⁴ C_{dl} is the double-layer capacitance, which can be determined from the cyclic voltammetry in a non-Faradic region at different scan rates ranging from 20 mV s⁻¹ to 120 mV s⁻¹:

$$C_{\text{dl}} = \frac{\Delta j \times S}{2 \nu} \quad \#(6)$$

where Δj is the difference between the anodic current density (j_a) and the cathodic current density (j_c) at a certain potential, S is the electrode area, ν is the scan rate.

Calculation of apparent rate constant:

$$k_{\text{ap}} t = - \ln\left(\frac{c_t}{c_0}\right) \quad \#(7)$$

where k_{ap} is apparent rate constant, t is reaction time, c_0 (mmol L⁻¹) is the initial concentration of NO₃⁻, and c_t (mmol L⁻¹) is the concentration of NO₃⁻ after a period of electrolysis.

Calculation of apparent activation energy:

$$\frac{\partial(\log(Y_{\text{NH}_3}))}{\partial(1/T)} = \frac{E_a}{8.314} \#(8)$$

where E_a is apparent activation energy, T (K) stands for reaction temperature.

Isotope labelling experiments: K^{15}NO_3 was used as the N source to perform the isotopic labelling experiments. The solution of 1.0 M KOH and 0.1 M K^{15}NO_3 was used as electrolyte. After electrolysis, 1 mL of electrolyte was extracted from electrolytic cell and mixed with 2 mL of 0.5 M H_2SO_4 , 0.1 mL of D_2O (containing 4.4 mg mL^{-1} of $\text{C}_4\text{H}_4\text{O}_4$). Subsequently, the above mixed solution was transferred to NMR tube for ^1H NMR test. A series of standard $^{15}\text{NH}_4\text{Cl}$ solution with known concentrations was tested for calibration.

***In-situ* Raman spectroscopy measurements:** *In-situ* Raman spectroscopy measurements were performed utilizing the LabRAM HR800 with a 532 nm laser. A homemade three-electrode configuration was employed. The solution of 1.0 M KOH and 0.1 M NO_3^- was used for electrolyte. All spectra were gathered during chronoamperometric experiments at different potentials.

***In-situ* attenuated total reflection Fourier transformed infrared (ATR-FTIR) measurements:** *In-situ* ATR-FTIR measurements were performed on a Thermo Scientific Nicolet 6700 spectrometer with a highly sensitive Mercury-Cadmium-Telluride (MCT) detector cooled with liquid nitrogen. Au-plated Si crystal was used as substrate for catalysts, Hg/HgO and Pt wire served as reference and counter electrodes, respectively. All spectra were obtained during the chronoamperometric tests for 4 min at different potentials in 1.0 M KOH and 0.1 M NO_3^- .

Computational details: The calculations were conducted using the Vienna *Ab initio* Simulation Package (VASP) software, employing a first-principles methodology rooted in density functional theory (DFT).⁵ The projective augmented wave (PAW) method delineates the interplay between valence and core electrons, whereas the exchange-correlation functional is characterized by the generalized gradient approximation (GGA) functional, specifically the Perdew-Burke-Ernzerhof (PBE) functional.^{6,7} An energy cutoff of 400 eV was established for the plane-wave basis set. Convergence was

achieved when the energy difference fell below 10^{-5} eV and the force threshold reached 0.03 eV/Å. For improved structural optimization, the Brillouin zone was sampled using the $3 \times 3 \times 1$ Monkhorst-Pack mesh. To accurately capture van der Waals interactions, the DFT-D3 method was incorporated into the calculations.⁸ For the construction of structural models, a vacuum layer of 15 Å along the z-axis was included. TiO_2 (110) and Fe (110), as the most thermodynamically stable crystal facets, were chosen.^{9,10} All the slabs consist of 4 layers. The heterostructure of TiO_2/Fe was simulated by positioning 1-layered Fe on 3-layered TiO_2 due to the ultralow Fe content revealed by EDS. During the optimization process, the atoms in the bottom layer of the slab were constrained at their bulk positions, while the top two layers were fully relaxed. The following equation allows for the calculation of the Gibbs free energy change for each intermediary process:

$$\Delta G = \Delta E + \Delta \text{ZPE} - T\Delta S \#(9)$$

where ΔE is the value of the reaction energy difference, ΔZPE is the zero-point energy change, and ΔS is the entropy change.

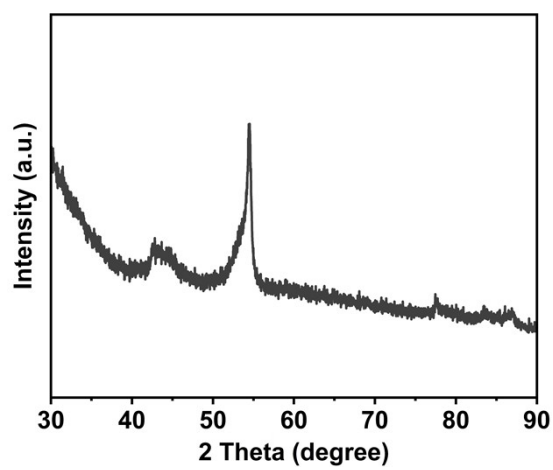


Fig. S1. XRD pattern of bare CP.

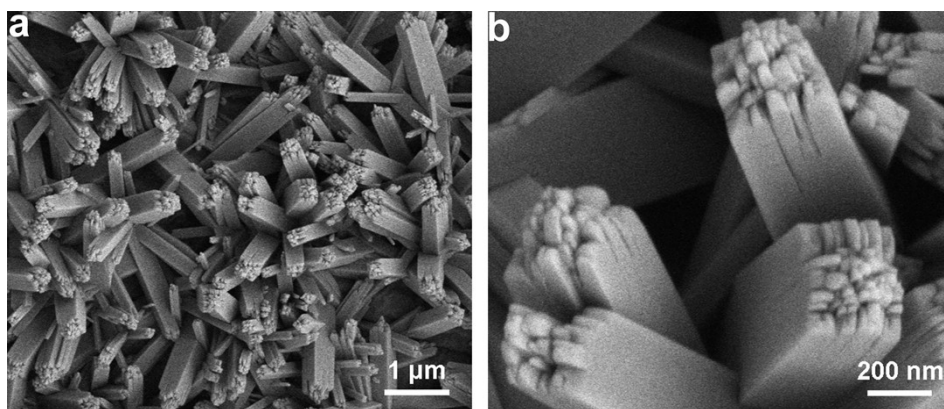


Fig. S2. SEM images of TiO₂ at (a) low and (b) high magnification.

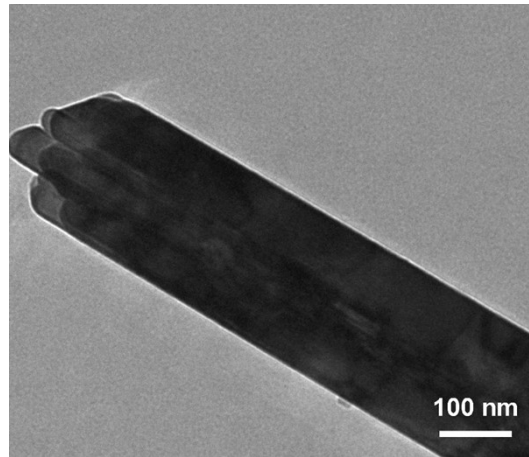


Fig. S3. TEM image of TiO₂.

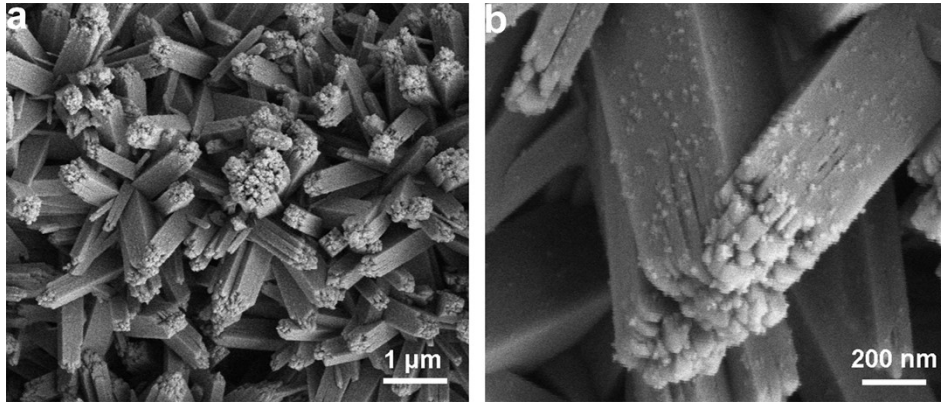


Fig. S4. SEM images of TiO_2/Fe at (a) low and (b) high magnification.

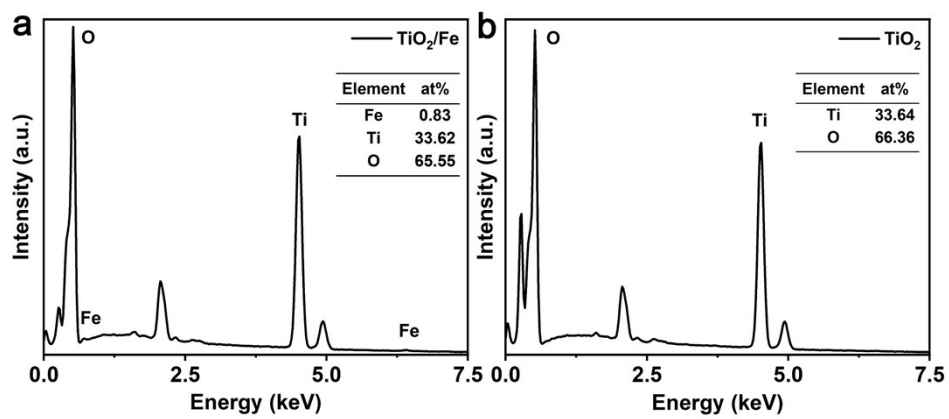


Fig. S5. EDS spectra of (a) TiO₂/Fe and (b) TiO₂.

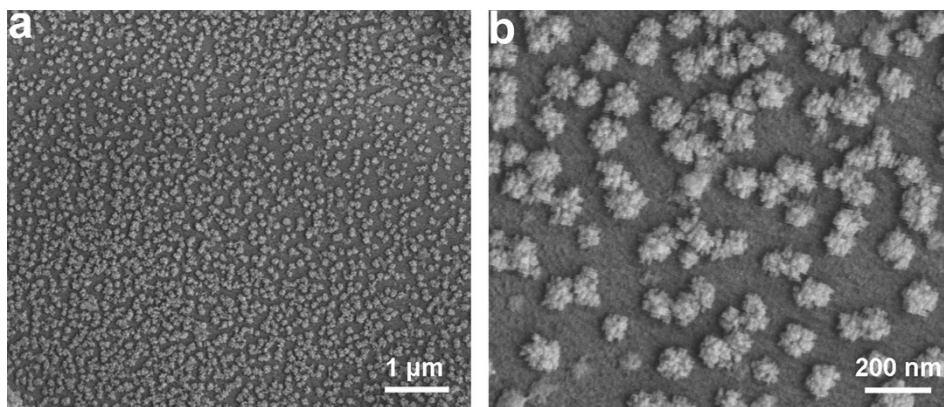


Fig. S6. SEM images of Fe at (a) low and (b) high magnification.

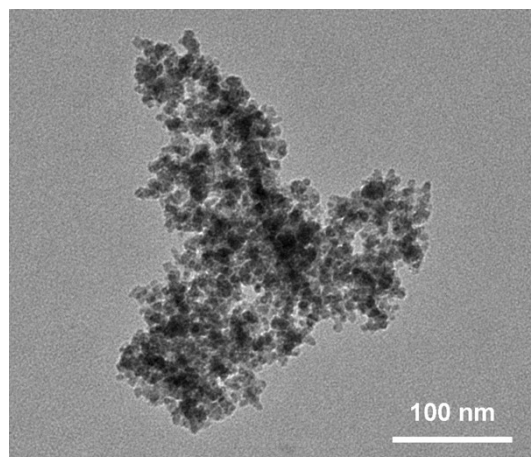


Fig. S7. TEM image of Fe.

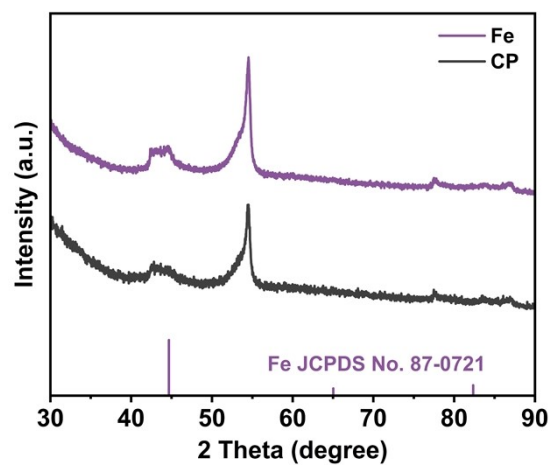


Fig. S8. XRD patterns of Fe/CP and bare CP.

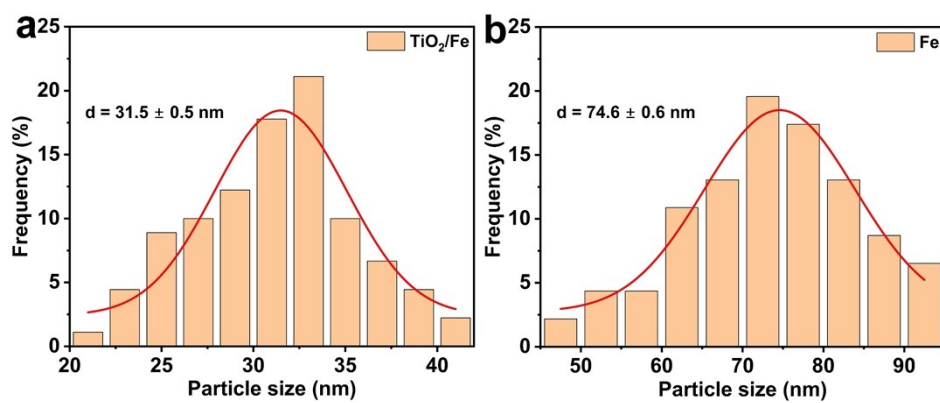


Fig. S9. The size distribution histograms of Fe nanoparticles in (a) TiO₂/Fe and (b) Fe, measured from Fig. S4b and Fig. S6b.

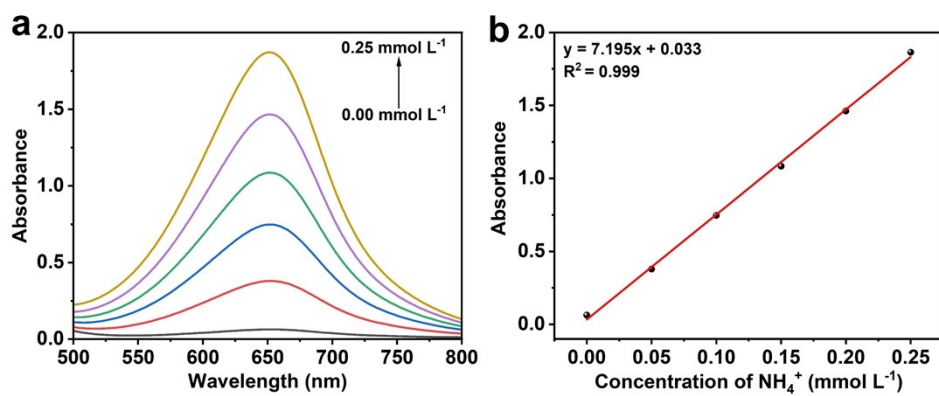


Fig. S10. (a) UV-Vis absorption spectra of NH_4^+ solution with different concentrations.

(b) Calibration curve used for the determination of NH_4^+ concentrations.

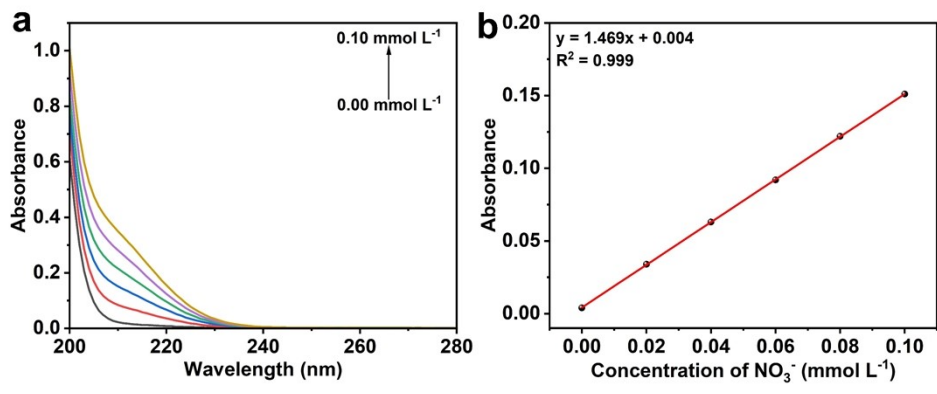


Fig. S11. (a) UV-Vis absorption spectra of acidified NO_3^- solutions with different concentrations. (b) Calibration curve used for the determination of NO_3^- concentrations.

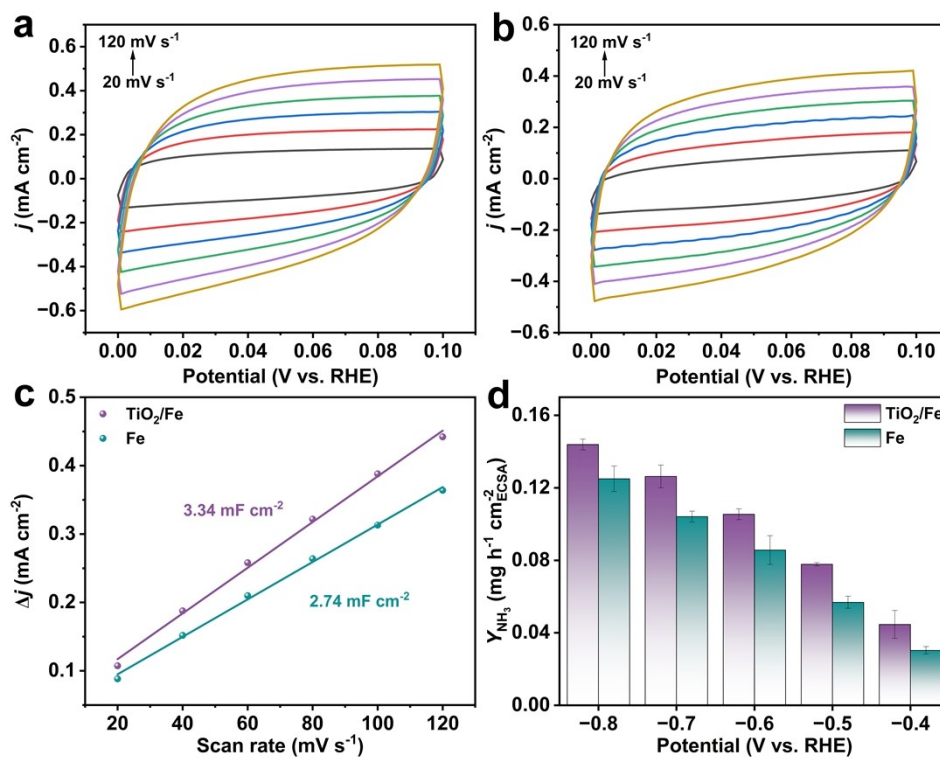


Fig. S12. CV curves of (a) TiO₂/Fe, (b) Fe at different scan rates ranging from 20 mV s⁻¹ to 120 mV s⁻¹. (c) Linear fittings of capacitive current densities against the scan rates of TiO₂/Fe and Fe. (d) ECSA-normalized Y_{NH_3} of TiO₂/Fe and Fe at different potentials.

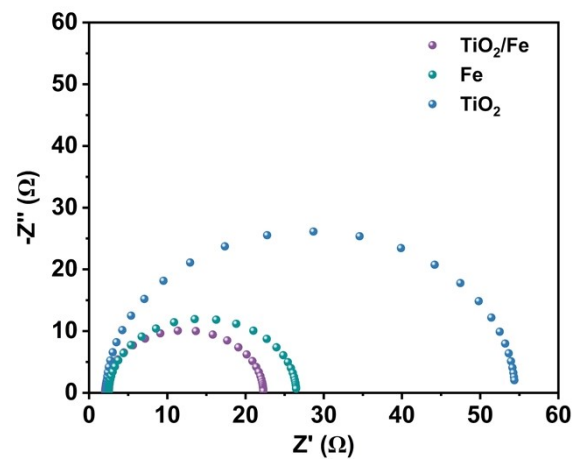


Fig. S13. Nyquist plots of TiO_2/Fe , Fe, and TiO_2 .

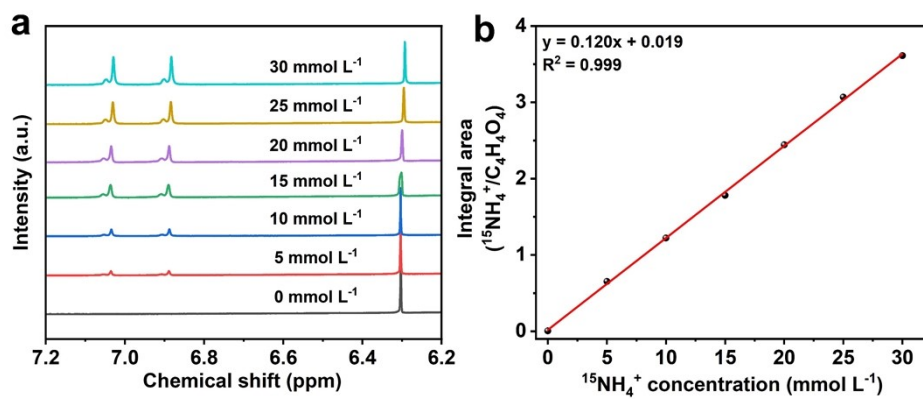


Fig. S14. (a) ^1H NMR spectra of standard $^{15}\text{NH}_4^+$ solutions with different concentrations. (b) Calibration curve used for the determination of $^{15}\text{NH}_4^+$ concentrations.

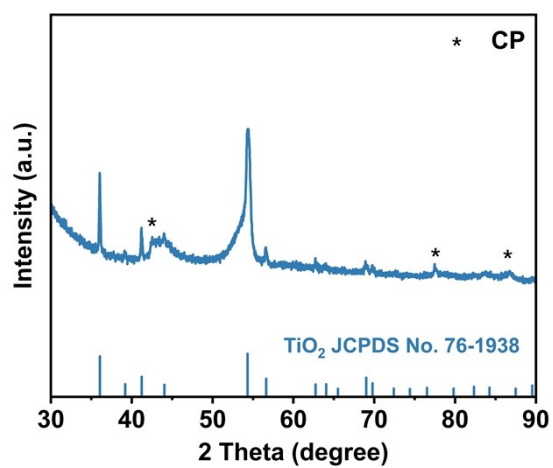


Fig. S15. XRD pattern of TiO₂/Fe supported on CP after 10 consecutive recycling tests.

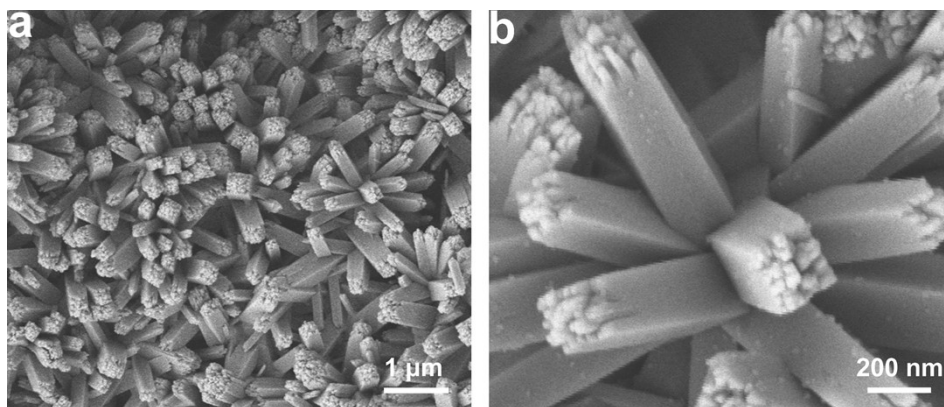


Fig. S16. SEM images of TiO₂/Fe at (a) low and (b) high magnification after 10 consecutive recycling tests.

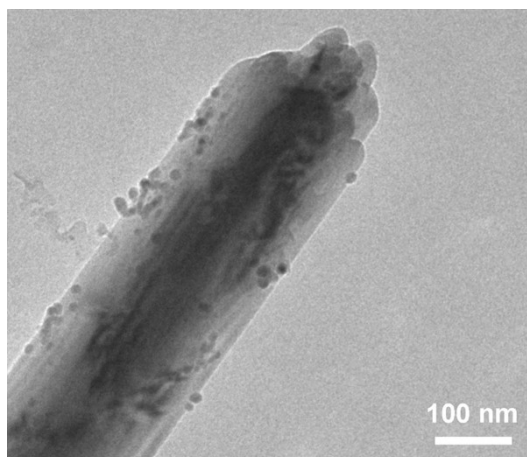


Fig. S17. TEM image of TiO₂/Fe after 10 consecutive recycling tests.

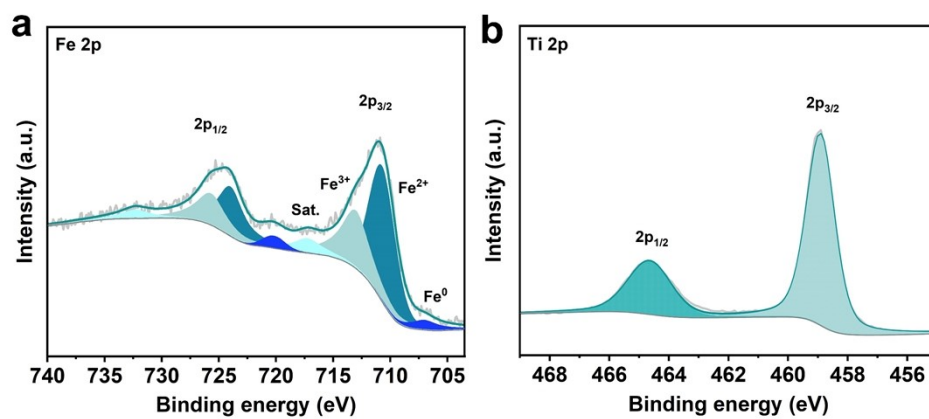


Fig. S18. XPS spectra of (a) Fe 2p and (b) Ti 2p for TiO₂/Fe after 10 consecutive recycling tests.

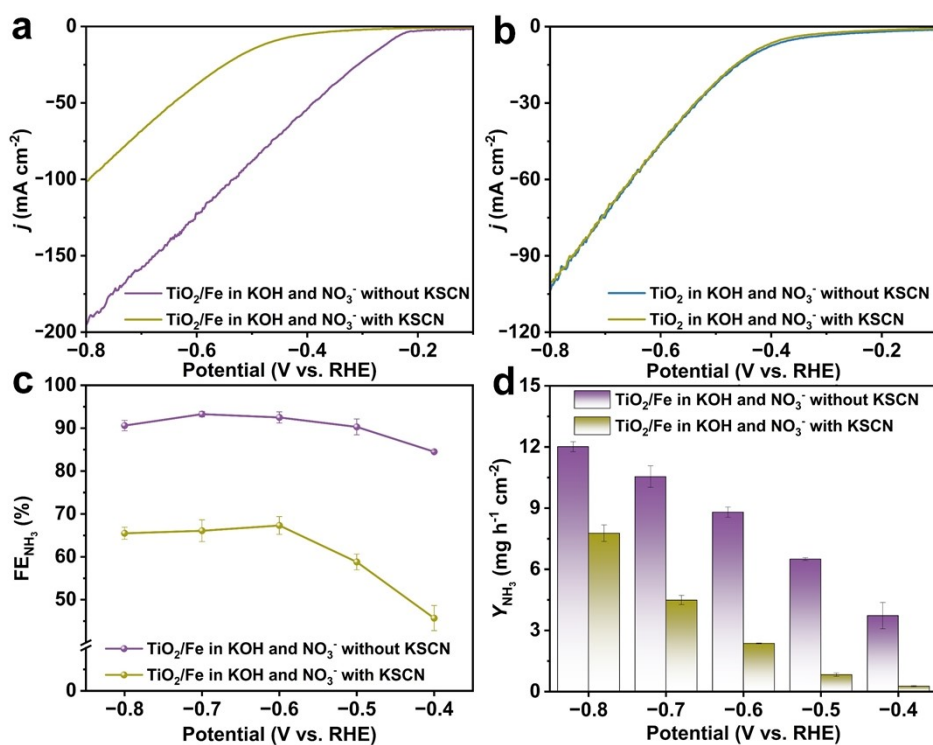


Fig. S19. LSV curves of (a) TiO₂/Fe, (b) TiO₂ in 1.0 M KOH and 0.1 M NO₃⁻ with and without 10 mM KSCN. (c) FE_{NH_3} and (d) Y_{NH_3} of TiO₂/Fe in 1.0 M KOH and 0.1 M NO₃⁻ with 10 mM KSCN at different potentials.

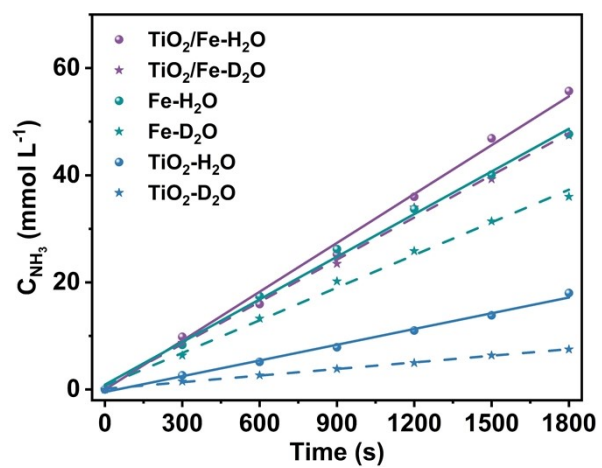


Fig. S20. Time-dependent concentration changes of NH_3 on TiO_2/Fe , Fe , and TiO_2 using H_2O or D_2O as solvent.

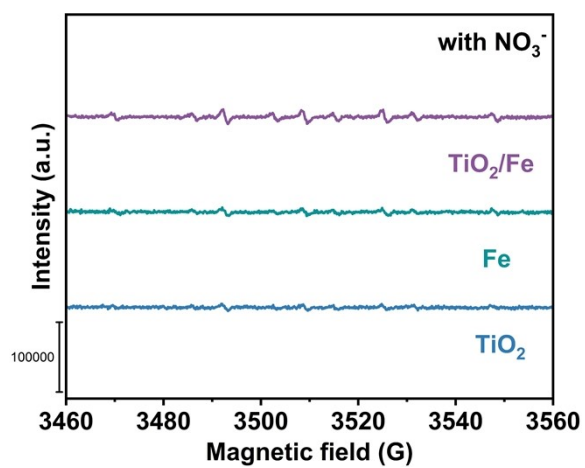


Fig. S21. ESR spectra of the electrolytes obtained after 3 min's electrolysis at -0.7 V by TiO₂/Fe, Fe, and TiO₂ in 1.0 M KOH with 0.1 M NO₃⁻.

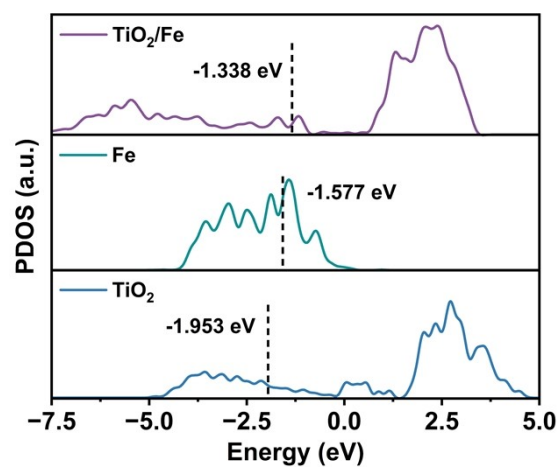


Fig. S22. PDOS profiles of TiO_2/Fe , Fe, and TiO_2 , the dashed lines represent the d-band center.

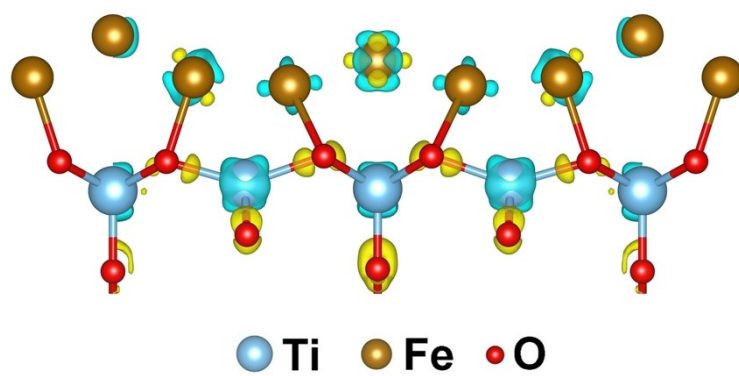


Fig. S23. Differential charge density profile of TiO₂/Fe. Yellow and cyan regions suggest the accumulation and depletion of electrons, respectively.

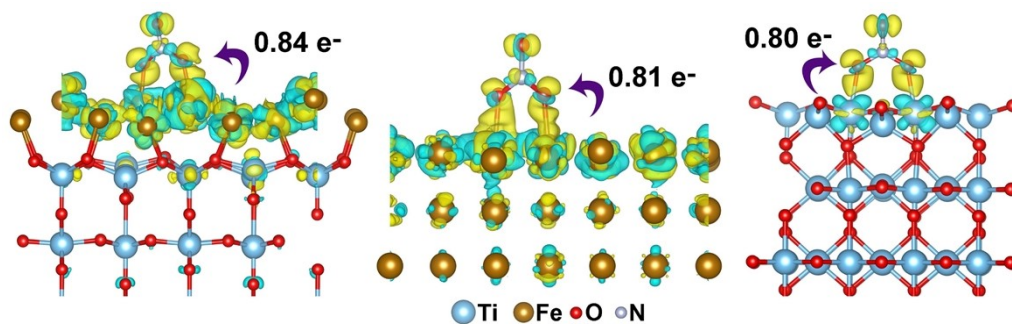


Fig. S24. Charge density difference of *NO_3 adsorption on TiO_2/Fe , Fe , and TiO_2 . The numbers represent charge transferred, and yellow and cyan regions suggest the accumulation and depletion of electrons, respectively.

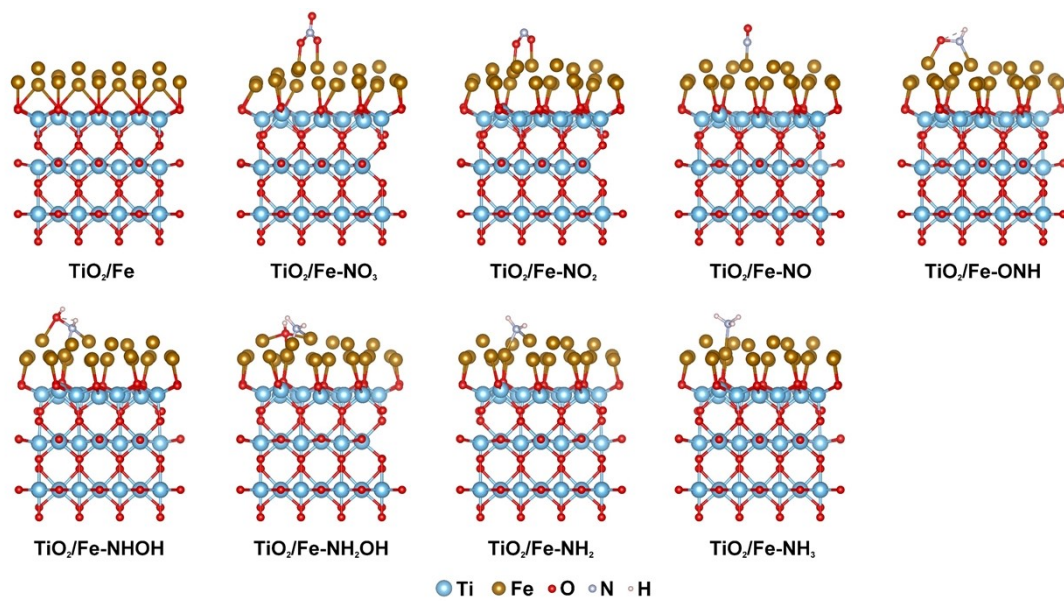


Fig. S25. Optimized structure models of TiO_2/Fe with absorbed NRA intermediates.

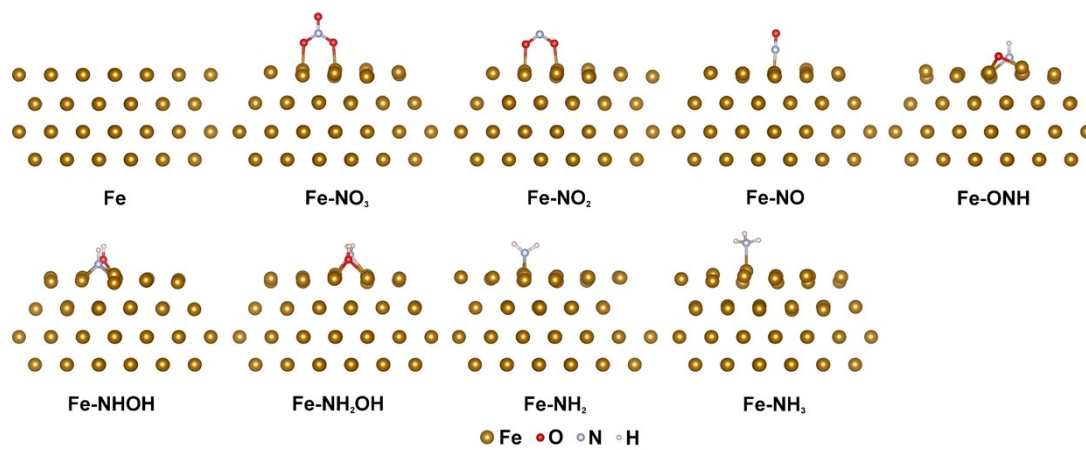


Fig. S26. Optimized structure models of Fe with absorbed NRA intermediates.

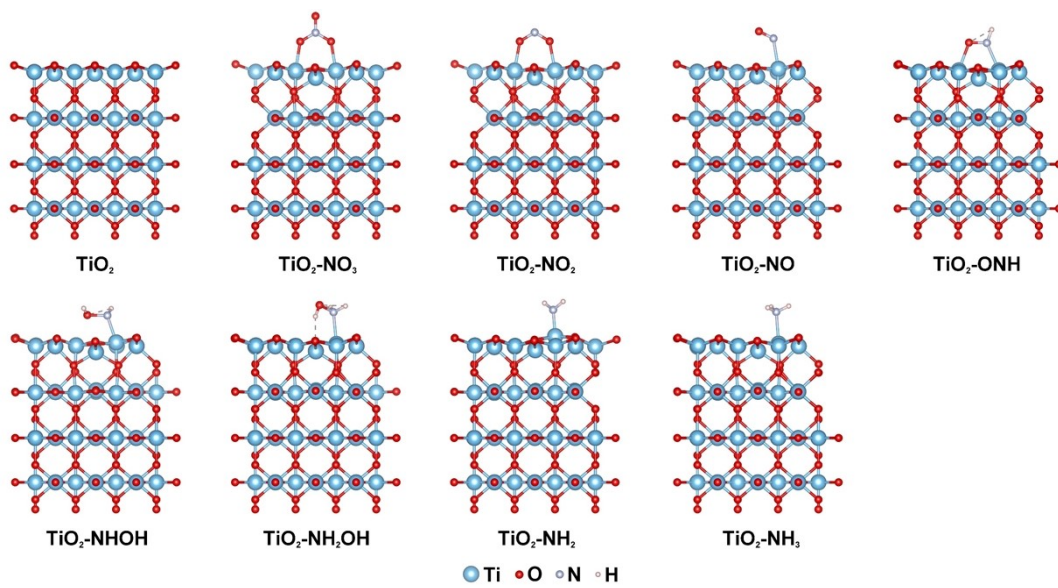


Fig. S27. Optimized structure models of TiO_2 with absorbed NRA intermediates.

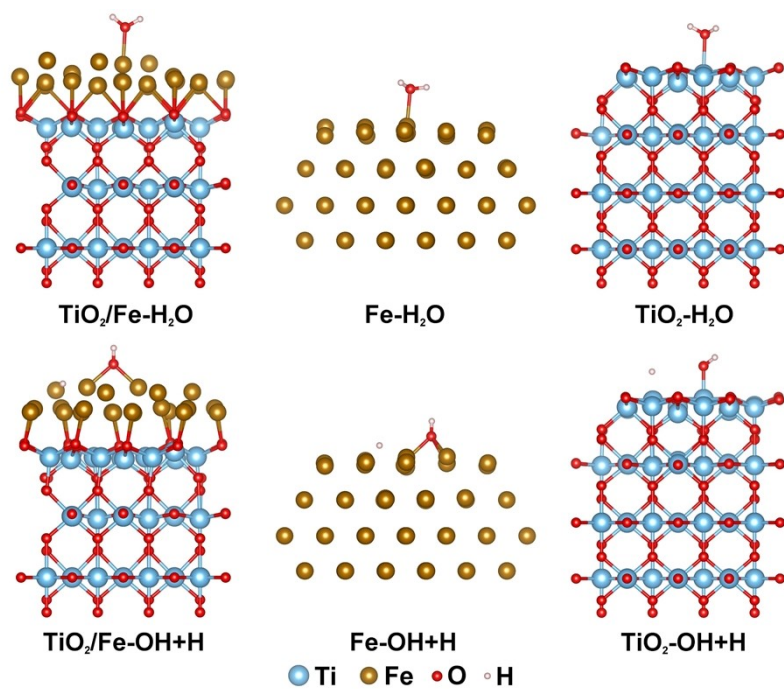


Fig. S28. Optimized structure models of TiO₂/Fe, Fe and TiO₂ with absorbed H₂O and OH+H intermediates.

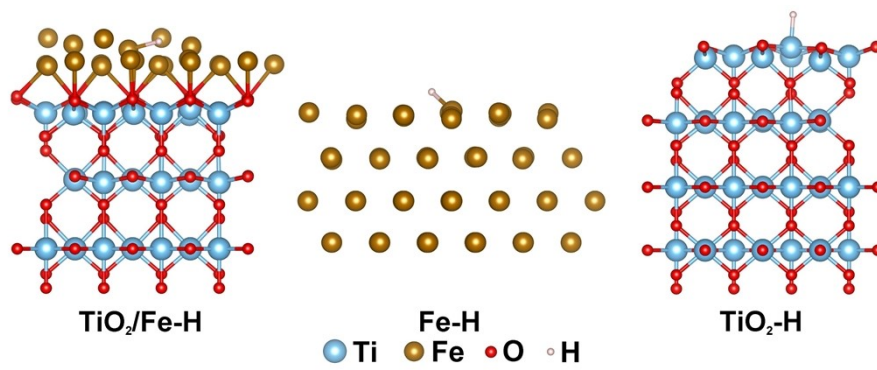


Fig. S29. Optimized structure models of TiO_2/Fe , Fe and TiO_2 with absorbed $^*\text{H}$ intermediates.

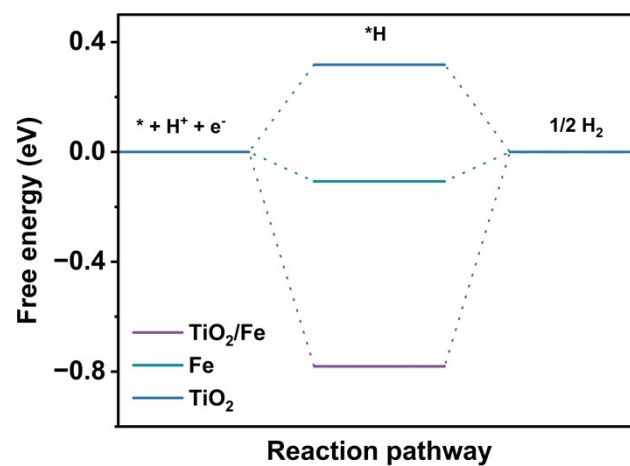


Fig. S30. Free energy diagram of HER on TiO₂/Fe, Fe, and TiO₂.

Table S1. Comparison of NRA performance for TiO₂/Fe and other electrocatalysts under ambient conditions.

Catalyst	Electrolyte	Performance	Ref.
TiO ₂ /Fe	1 M KOH + 0.1 M NO ₃ ⁻	Y_{NH_3} : 11.96 mg h ⁻¹ cm ⁻² at -0.8 V FE_{NH_3} : 93.3% at -0.7 V	This work
Pd/TiO ₂	1 M LiCl + 0.25 M LiNO ₃	Y_{NH_3} : 1.12 mg h ⁻¹ cm ⁻² at -0.8 V FE_{NH_3} : 92.1% at -0.7 V	11
Au-NC/TiO ₂	0.2 M Na ₂ SO ₄ + 0.05 M NaNO ₃	Y_{NH_3} : 1.92 mg h ⁻¹ cm ⁻² at -0.6 V FE_{NH_3} : 91% at -0.6 V	12
FePc/TiO ₂	0.1 M KOH + 0.5 M KNO ₃	Y_{NH_3} : 17.4 mg h ⁻¹ cm ⁻² at -0.65 V FE_{NH_3} : 90.6% at -0.25 V	13
Mo/TiO ₂ -M	0.05 M Na ₂ SO ₄ + 0.1 M NO ₃ ⁻	Y_{NH_3} : 5.18 mg h ⁻¹ cm ⁻² at -1.1 V FE_{NH_3} : 88.05% at -0.8 V	14
Fe-SAC	0.1 M K ₂ SO ₄ + 0.5 M NO ₃ ⁻	Y_{NH_3} : 7.82 mg h ⁻¹ cm ⁻² at -0.85 V FE_{NH_3} : 75% at -0.66 V	15
Co/TiO ₂ NSs	1.0 M PBS + 0.4 M NO ₃ ⁻	Y_{NH_3} : 5.92 mg h ⁻¹ cm ⁻² at -1.12 V FE_{NH_3} : 97.4% at -0.72 V	16
FeCoNiAlTi HEA NPs	0.2 M K ₂ SO ₄ + 0.05 M KNO ₃	Y_{NH_3} : 0.52 mg h ⁻¹ cm ⁻² at -0.5 V FE_{NH_3} : 95.2% at -0.5 V	17
Fe/Cu-NG	0.1 M KOH + 0.1 M KNO ₃	Y_{NH_3} : 4.41 mg h ⁻¹ cm ⁻² at -0.5 V FE_{NH_3} : 92.5% at -0.3 V	18
Co ₁ Ni ₂ Cu ₁ Mn ₁ Fe ₁	0.1 M KOH + 0.05 M KNO ₃	Y_{NH_3} : 3.25 mg h ⁻¹ cm ⁻² at -0.6 V FE_{NH_3} : 92% at -0.6 V	19

Fe@Cu ₁ FeO _x	0.1 M K ₂ SO ₄ + 0.07 M KNO ₃	Y_{NH_3} : 1.98 mg h ⁻¹ cm ⁻² at -0.65 V FE_{NH_3} : 95.4% at -0.65 V	20
Fe/Ni ₂ P	0.2 M K ₂ SO ₄ + 0.05 M KNO ₃	Y_{NH_3} : 4.17 mg h ⁻¹ cm ⁻² at -0.4 V FE_{NH_3} : 94.3% at -0.4 V	21
FeNi ₃	1 M KOH + 0.1 M KNO ₃	Y_{NH_3} : 6.48 mg h ⁻¹ cm ⁻² at -0.45 V FE_{NH_3} : 95.5% at -0.35 V	22
Fe-V ₂ O ₅	1 M KOH + 0.1 M NO ₃ ⁻	Y_{NH_3} : 12.5 mg h ⁻¹ cm ⁻² at -0.7 V FE_{NH_3} : 97.1% at -0.7 V	23

References

- 1 Y. Lu, C.-Y. Chiang and E. Huang, *Appl. Mater. Today*, 2020, **20**, 100707.
- 2 E. Hosono, S. Fujihara, K. Kakiuchi and H. Imai, *J. Am. Chem. Soc.*, 2004, **126**, 7790-7791.
- 3 W. Guo, C. Xu, X. Wang, S. Wang, C. Pan, C. Lin and Z. L. Wang, *J. Am. Chem. Soc.*, 2012, **134**, 4437-4441.
- 4 Y. Zhang, C. Ma, X. Zhu, K. Qu, P. Shi, L. Song, J. Wang, Q. Lu and A.-L. Wang, *Adv. Energy Mater.*, 2023, **13**, 2301492.
- 5 W. Kohn and L. J. Sham, *Phys. Rev.*, 1965, **140**, A1133-1138.
- 6 G. Kresse and D. Joubert, *Phys. Rev. B*, 1999, **59**, 1758-1775.
- 7 J. P. Perdew, K. Burke and M. Ernzerhof, *Phys. Rev. Lett.*, 1996, **77**, 3865-3868.
- 8 S. Grimme, J. Antony, S. Ehrlich and H. Krieg, *J. Chem. Phys.*, 2010, **132**, 154104.
- 9 U. Diebold, *Surf. Sci. Rep.*, 2003, **48**, 53-229.
- 10 L. Vitos, A. V. Ruban, H. L. Skriver and J. Kollár, *Surf. Sci.*, 1998, **411**, 186-202.
- 11 Y. Guo, R. Zhang, S. Zhang, Y. Zhao, Q. Yang, Z. Huang, B. Dong and C. Zhi, *Energy Environ. Sci.*, 2021, **14**, 3938-3944.
- 12 M. Yang, T. Wei, J. He, Q. Liu, L. Feng, H. Li, J. Luo and X. Liu, *Nano Res.*, 2024, **17**, 1209-1216.
- 13 R. Zhang, C. Li, H. Cui, Y. Wang, S. Zhang, P. Li, Y. Hou, Y. Guo, G. Liang, Z. Huang, C. Peng and C. Zhi, *Nat. Commun.*, 2023, **14**, 8036.
- 14 H. Chen, W. Hu, T. Ma, Y. Pu, S. Wang, Y. Wang and S. Yuan, *Molecules*, 2024, **29**, 2782.
- 15 Z.-Y. Wu, M. Karamad, X. Yong, Q. Huang, D. A. Cullen, P. Zhu, C. Xia, Q. Xiao, M. Shakouri, F.-Y. Chen, J. Y. Kim, Y. Xia, K. Heck, Y. Hu, M. S. Wong, Q. Li, I. Gates, S. Siahrostami and H. Wang, *Nat. Commun.*, 2021, **12**, 2870.

- 16 Y.-T. Xu, Y. Han, D. K. Sam and Y. Cao, *J. Mater. Chem. A*, 2022, **10**, 22390-22398.
- 17 R. Zhang, Y. Zhang, B. Xiao, S. Zhang, Y. Wang, H. Cui, C. Li, Y. Hou, Y. Guo, T. Yang, J. Fan and C. Zhi, *Angew. Chem., Int. Ed.*, 2024, **63**, e202407589.
- 18 S. Zhang, J. Wu, M. Zheng, X. Jin, Z. Shen, Z. Li, Y. Wang, Q. Wang, X. Wang, H. Wei, J. Zhang, P. Wang, S. Zhang, L. Yu, L. Dong, Q. Zhu, H. Zhang and J. Lu, *Nat. Commun.*, 2023, **14**, 3634.
- 19 W. Qiu, Y. Guo, X.-Z. Fu and J.-L. Luo, *Adv. Funct. Mater.*, 2025, **35**, 2415970.
- 20 B. Zhou, L. Yu, W. Zhang, X. Liu, H. Zhang, J. Cheng, Z. Chen, H. Zhang, M. Li, Y. Shi, F. Jia, Y. Huang, L. Zhang and Z. Ai, *Angew. Chem., Int. Ed.*, 2024, **63**, e202406046.
- 21 R. Zhang, Y. Guo, S. Zhang, D. Chen, Y. Zhao, Z. Huang, L. Ma, P. Li, Q. Yang, G. Liang and C. Zhi, *Adv. Energy Mater.*, 2022, **12**, 2103872.
- 22 K. Qu, X. Zhu, L. Song, J. Wang, Y. Gong, X. Liu, S. Yuan, Q. Lu, Y. Yu and A.-L. Wang, *Chem. Eng. J.*, 2025, **510**, 161814.
- 23 N. Zhang, G. Zhang, P. Shen, H. Zhang, D. Ma and K. Chu, *Adv. Funct. Mater.*, 2023, **33**, 2211537.